Experimental achievement and signatures of ignition at the NIF

A. B. Zylstra,[1, *] A. L. Kritcher,[1] O. A. Hurricane,[1] D. A. Callahan,[1] J. E. Ralph,[1] D. T. Casey,[1] A. Pak,[1] O. L. Landen,[1] B. Bachmann,[1] K. L. Baker,[1] L. Berzak Hopkins,[1] S. D. Bhandarkar,[1] J. Biener,[1] R. M. Bionta,[1] N. W. Birge,[2] T. Braun,[1] T. M. Briggs,[1] P. M. Celliers,[1] H. Chen,[1] C. Choate,[1] D. S. Clark,[1] L. Divol,[1] T. Döppner,[1] D. Fittinghoff,[1] M. J. Edwards,[1] M. Gatu Johnson,[3] N. Gharibyan,[1] S. Haan,[1] K. D. Hahn,[1] E. Hartouni,[1] D. E. Hinkel,[1] D. D. Ho,[1] M. Hohenberger,[1] J. P. Holder,[1] H. Huang,[4] N. Izumi,[1] J. Jeet,[1] O. Jones,[1] S. M. Kerr,[1] S. F. Khan,[1] H. Geppert Kleinrath,[2] V. Geppert Kleinrath,[2] C. Kong,[4] K. M. Lamb,[2] S. Le Pape,[5] N. C. Lemos,[1] J. D. Lindl,[1] B. J. MacGowan,[1] A. J. Mackinnon,[1] A. G. MacPhee,[1] E. V. Marley,[1] K. Meaney,[2] M. Millot,[1] A. S. Moore,[1] K. Newman,[1] J.-M. G. Di Nicola,[1] A. Nikroo,[1] R. Nora,[1] P. K. Patel,[1, †] N. G. Rice,[4] M. S. Rubery,[1] J. Sater,[1] D. J. Schlossberg,[1] S. M. Sepke,[1] K. Sequoia,[4] S. J. Shin,[1] M. Stadermann,[1] S. Stoupin,[1] D. J. Strozzi,[1] C. A. Thomas,[6] R. Tommasini,[1] C. Trosseille,[1] E. R. Tubman,[1] P. L. Volegov,[2] C. R. Weber,[1] C. Wild,[7] D. T. Woods,[1] S. T. Yang,[1] and C. V. Young[1]

[1]*Lawrence Livermore National Laboratory, P.O. Box 808, Livermore, California 94551-0808, USA*
[2]*Los Alamos National Laboratory, Mail Stop F663, Los Alamos, New Mexico 87545, USA*
[3]*Massachusetts Institute of Technology, Cambridge, Massachusetts 02139, USA*
[4]*General Atomics, San Diego, California 92186, USA*
[5]*Laboratoire pour l'utilisation des Lasers Intenses chez École Polytechnique, F-91128 Palaiseau cedex, France*
[6]*Laboratory for Laser Energetics, University of Rochester, Rochester, New York 14623, USA*
[7]*Diamond Materials Gmbh, 79108 Freiburg, Germany*
(Dated: June 27, 2022)

An inertial fusion implosion on the National Ignition Facility, conducted on August 8th 2021 (N210808), recently produced more than a megajoule of fusion yield and passed Lawson's criterion for ignition [Phys. Rev. Lett. XX, YY (2022)]. Herein we describe the experimental improvements that enabled N210808 and present the first experimental measurements from an igniting plasma in the laboratory. Ignition metrics like the product of hot-spot energy and pressure squared, in the absence of self-heating, increased by $\sim 35\%$, leading to record values and an enhancement from previous experiments in the hot spot energy ($\sim 3\times$), pressure ($\sim 2\times$), and mass ($\sim 2\times$). These results are consistent with self-heating dominating other power balance terms. The burn rate increases by an order of magnitude after peak compression, and the hot spot conditions show clear evidence for burn propagation into the dense fuel surrounding the hot spot. These novel dynamics and thermodynamic properties have never been observed on prior inertial fusion experiments.

The pursuit of nuclear fusion in the laboratory requires the generation of extreme conditions, especially for inertial confinement fusion (ICF). ICF uses high-power drivers to rapidly compress and heat the deuterium-tritium (DT) fuel to fusion conditions[1]; here, we discuss laser-driven indirect drive [2], in which the laser energy is converted to a thermal x-ray bath inside a 'hohlraum', which produces a high ablation pressure on the outer surface of a fuel-containing capsule, imploding it. This process is inefficient, with only a small fraction ($\sim 1\%$) of the initial laser energy coupled into the fuel's internal energy through PdV work of the implosion. Heating a large fuel mass to temperatures where the fusion power exceeds bremsstrahlung losses ($\gtrsim 4.3$ keV for 'clean' DT without high-Z mix) is therefore energetically prohibitive, so the implosion is designed to generate a smaller mass central 'hot spot' in which fusion can begin to burn and subsequently propagate into a larger fuel mass. For burn propagation, enabling high yield, to occur, the hot-spot must enter regimes where the fusion self-heating becomes dominant. Experiments at the National Ignition Facility [3] recently entered into the 'burning plasma' regime[4, 5], in which the fusion self-heating is greater than the PdV work. These experiments generated fusion yields up to 170kJ, substantially less than the 1.9MJ laser energy, and were still in a regime where the self-heating from fusion did not exceed loss mechanisms. Beyond a burning plasma the next novel physical regime is an 'ignited' plasma in which self-heating is greater than all loss mechanisms leading to a thermonuclear instability[6].

The NIF experiment N210808[7] produced a fusion yield of 1.37 MJ, $8\times$ higher than its predecessor, passing scientific criteria for ignition[8]. Here we describe the experimental development that led to this result and present novel experimental signatures for ignition and burn propagation, which have never before been observed in laboratory experiments. The paper is organized as follows: Section I describes the experimental improvements made that enabled N210808's record level of performance, Section II describes the measurement and inference methodology used, and Section III explores novel data-based signatures of ignition, and the paper is concluded in Section IV.

* zylstra1@llnl.gov
† now at Focused Energy Inc., 11525-B Stonehollow Drive, Suite 200, Austin TX 78758 USA
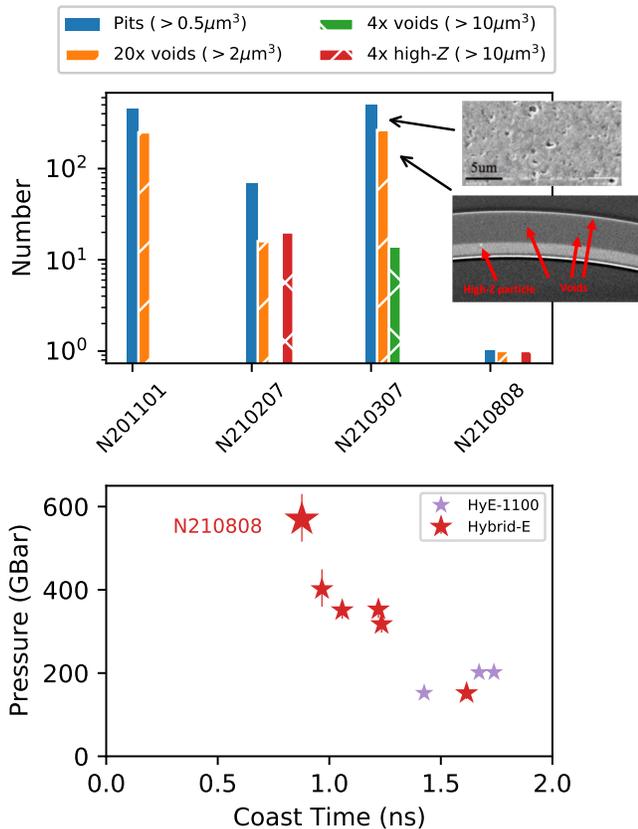
FIG. 1. Improvements made in the N210808 experiment included higher-quality capsules (top, showing the number of 'pits', 'voids', and high-Z inclusions compared to predecessor experiments), and lower coast time (bottom, see Ref. 9 for details of the design change made to enable the reduced coast time). Compared to the predecessors, the pressure of N210808 increased dramatically, as expected for the reduced coast[10]. Inset at top are SEM and tomography images of pits and voids, respectively, in previous capsule batches.

I. EXPERIMENTAL IMPROVEMENTS

N210808 was an experiment conducted using the 'Hybrid E' design, see Kritcher et al. (Ref. 9). The 'Hybrid' strategy[11] aimed to increase the capsule scale, which is advantageous for performance if other implosion parameters are preserved; the Hybrid E approach to solving this challenge was to use a smaller case-to-capsule ratio (CCR, the ratio of the hohlraum radius to capsule radius) to improve hohlraum efficiency while re-introducing the use of cross-beam energy transfer (CBET) to control drive symmetry[12, 13]. Initial Hybrid E experiments showed dramatically improved energy coupling to the capsule (by $\sim 50 - 60\%$), at the cost of reduced stagnation pressure[12]. These initial experiments (purple stars in Fig. 1) were limited by long 'coast time', which is the duration between when the radiation drive on the implosions begins to decrease after the laser turns

off at the time of peak compression, and suffered mix from capsule defects[12, 14]. The coast time on those initial shots was ~ 1.4 ns from 90% peak radiation temperature (T_{rad}) to peak compression, or ~ 1.6 ns from the laser turning off to peak compression (as shown in Fig. 1). Such long coast times are deleterious because the in-flight shell can decompress and the shell deceleration occurs over a longer duration, reducing stagnation pressure[10, 15, 16] because of the reduced rate at which kinetic energy is converted to internal energy. A metric for ignition is the product of hot-spot energy and pressured squared (EP^2)[17] so increasing energy coupling at the cost of pressure is not advantageous[18]. Reducing the coast time to below $\sim 1 - 1.2$ ns was therefore key to advancing Hybrid E implosions into the burning-plasma regime[5]. The previous experimental campaigns had observed clear instances in which capsule quality reduced performance through higher levels of mix[12–14], motivating continued improvement in the target quality. These two improvements in the coast time and capsule quality are shown in Fig. 1. Lastly, efforts are ongoing to improve the low-mode drive symmetry on the capsule. Herein we describe these three improvements made between the burning-plasma experiments described in Refs. 4, 5 and N210808.

A. Coast time

We implemented a reduced size laser entrance hole (LEH) to increase the hohlraum efficiency, which enabled an improved lower-coast implosion design [9]. Predecessor experiments to validate the modeling of the reduced LEH were conducted[19, 20] prior to a specific predecessor shot, N210601, to N210808 described here. Prior to DT layered experiments, simpler gas-filled symmetry capsule ('symcap') experiments are conducted to test aspects of the implosion design and benchmark our computational models[9]. Prior to N210808 a symcap experiment, N210601, was conducted to benchmark the drive and symmetry with the reduced LEH size and modified pulse shape. N210601 used the reduced-size 3.1mm LEH; from the original Hybrid-E beam pointing scheme[13], moving the outer beams in z for the smaller LEH was tested by the 'hohlraum scan' project[19, 20]. The redesigned pulse shape that enabled reduced coast time is described in Ref. 9. Compared to the full-energy DT experiment, the laser energy is reduced to 1.7MJ to reduce laser damage, with the pulse length maintained and peak power reduced correspondingly. Similarly, a symcap experiment N191118 served as a predecessor to the burning plasma DT experiments (N210207 and N210307). Here, we compare the data from these symcap shots.

Fig. 2 shows the delivered laser pulses (top) and radiation temperature (T_{rad}, bottom) versus time for the two symcap experiments; T_{rad} is measured with the Dante instrument[21]. The temporal dynamics here illustrate the key aspect of the hohlraum design change, as dis-
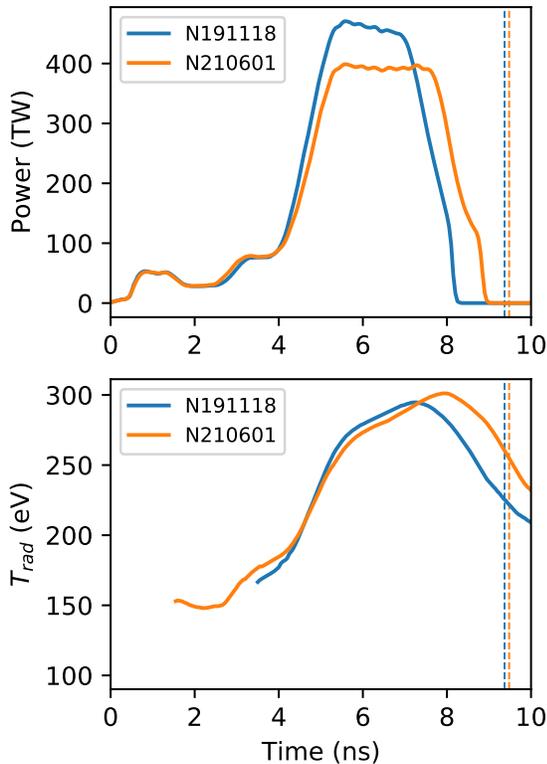
FIG. 2. Total laser power (top) and hohlraum radiation temperature (bottom) versus time for N191118 and N210601. The bang times for each are shown by the dashed lines in the corresponding color.

FIG. 3. X-ray self emission images from the two symcap experiments. The spatial scales are in μm. The color scale is identical for the two images, and the 17% emissivity contour is marked in white.

cussed in Ref. 9. With the smaller LEH the peak power can be reduced yet T_{rad} is maintained, being comparable until ~ 7.5 ns, when the N191118 pulse turns off and its T_{rad} begins decreasing. For N210601 in contrast, the laser pulse continues and T_{rad} continues to rise for an additional few hundred ps. By bang time, denoted by the vertical dashed curves and measured here with SPIDER[22], T_{rad} is significantly higher on N210601 indicating an expected improvement from the coast physics.

While improving the drive by hohlraum energetics, the implosion symmetry must be maintained, here by adjusting the amount of CBET using $\Delta\lambda$. By increasing $\Delta\lambda$ from 1.25Å(N191118) to 1.8Å(N210601), pre-shot expectations were that the symmetry would be maintained (see Ref. 9 end matter). Fig. 3 shows x-ray self emission images measured using penumbral imaging[23] on the two experiments. The mode 2 Legendre symmetry (P_2) is slightly prolate on both experiments: $P_2 = 12.5 \pm 3$ μm on N191118, and $P_2 = 4.7 \pm 0.4$ μm on N210601. The reduction in prolate P_2 is much less than would have been expected (see Ref. 9) without the compensating effect of the increased $\Delta\lambda$ and these experiments thus provided key benchmark data before the following DT experiments. The effect of reduced coast time for the DT layered experiment is discussed in Ref. 9 with the in-

creased pressure, inferred using the methodology in Ref. 24, at decreased coast time summarized in Fig. 1.

B. Capsule quality

Fabrication defects on the capsule used for an experiment, as well as engineering features of the target have been previously shown to seed hydrodynamic instabilities that subsequently inject capsule material into the fuel, reducing performance by increased radiative losses[25]. Engineering features are predominantly the capsule support 'tent' (a thin membrane which suspends the capsule at the center of the hohlraum) and the fill tube, through which the DT fuel enters the capsule. While the tent affected CH ablator experiments[26, 27] it is thought to be less impactful for HDC shells. In contrast we know that the fill tube injects a substantial amount of mix[28, 29] which can be mitigated by reducing its diameter[30, 31].

For the first time in the Hybrid-E campaign we reduced the diameter of the fill tube from 5 to 2 μm.

The capsule quality, specifically the number of 'pits' and 'voids', was also improved for the target used on N210808; these imperfections have been shown to cause mix in previous experiments[14]. Pits are missing material on the outer surface of the capsule, measured with optical microscopy, while 'voids' are regions of missing material within the shell wall, measured with x-ray computed tomography. In addition to voids high-Z particles included in the shell have been observed on some shells. Smaller voids are characterized in a 20× tomography, capturing 5% of the shell at high resolution, while larger voids are measured across the entire shell in a 4× tomography. Fig. 1 shows these metrics for shells used in previous work (Ref. 4) versus the shell used on N210808. A significant improvement in quality is clearly apparent; future work will further investigate the degree to which the improved capsule quality aided N210808 and the level at which these defects are tolerable for ignition experiments.

C. Low-mode symmetry

The drive symmetry on the capsule, especially at low mode numbers, must be controlled to achieve high implosion performance[32]. The mode-2 symmetry on N210808 was controlled using the data from N210601, described previously, plus simulation and quasi-empirical models (see Ref. 9). The impact of mode 1 asymmetries in capsule implosions on NIF has been studied extensively recently. Seeds for mode-1 asymmetry include laser non-uniformities[33], asymmetries in the initial fabricated capsule thickness[34], and from diagnostic windows placed in the hohlraum equator[35, 36]. The NIF laser power balance and accuracy have been improved recently[8] and capsule thickness asymmetries are controlled, within our ability, using pre-shot metrology. For the first time in the Hybrid-E campaign, N210808 used a new design of the equatorial diagnostic windows which reduces the flux asymmetry. The resulting asymmetry is characterized using either the resulting bulk hot spot velocity[37, 38] or with the isotropy of neutron emission[39, 40]. For the former, the apparent hot-spot velocity is comparable between the three experiments - 68 ± 7 km/s on N210808 vs 73 ± 12 (56 ± 9) km/s on N210207 (N210307). From the neutron emission isotropy, which is shown in Fig. 4, the variation in compression shell areal density (ρR) can be inferred[39, 41]. For these experiments the RMS variation in ρR is slightly smaller on N210808, 0.11 ± 0.02 g/cm^2 versus 0.15 ± 0.01 (0.13 ± 0.01) on the predecessor experiments N210207 (N210307). While this does not appear to be a dramatic improvement, the dynamics of low-mode asymmetry in the ignition regime are complicated by the highly dynamic explosion process driven by higher stagnation pressure and this physics will be explored in a future publication.

II. DATA AND INFERENCES

Conditions in the burning fuel of a NIF experiment are understood through a combination of directly measured and inferred quantities. Due to the substantially higher yield on N210808 compared to any previous NIF experiments some diagnostic data experienced saturation or required special processing. The nuclear yield is measured by both nuclear activation of Zr[42] and by magnetic spectroscopy of elastically-scattered charged particles in the Magnetic Recoil Spectrometer (MRS)[43, 44]; these instruments returned data as normal. The ion temperature (T_i) is inferred by the Doppler width[45] of emitted neutrons using neutron time of flight (NTOF) detectors [46, 47]; here the DD neutron measured temperature is typically used for inferred quantities[4, 24] and is unaffected by signal saturation. The DT ion temperature, measured by the MRS, is in agreement with the same measurement using electronic neutron time of flight, which relied on advanced fitting routines of clipped scope traces. The fuel areal density is inferred from the down-scattered ratio, which is measured by both NTOF and MRS. Nuclear burn width was measured by both the Gamma Reaction History (GRH)[48] and Gamma Cherenkov Detector (GCD)[49], while a redundant x-ray based measurement was unavailable due to saturation. The hohlraum radiation temperature history is measured by DANTE (a low energy resolution spectrometer) [21]. Key scalar quantities from these measurements are summarized in Table 1 of Ref. 8 and used for the analysis here.

Imaging of x-ray and neutron self-emission from the burning plasma is typically measured using a variety of systems, here time-integrated x-ray[23, 50] and neutron images[51, 52] are available plus one equatorial detector[53] recorded time-resolved x-ray images. The isotropy of neutron emission, correlated with the implosion low-mode symmetry, is measured using activation detectors[39, 40, 54] (shown in Fig. 4). The N210808 imaging data, shown in Fig. 5 compared to the two previous shots (N210207 and N210307), exhibits a larger volume by approximately a factor of 2. Note that in all shots a bright feature in the x-ray emission images, from the fill-tube jet[23, 31], is visible, but not at a level where the inferred size is substantially affected. In particular, the neutron self-emission region defines the hot spot where the key fusion power balance is taking place.

These measurements are used to produce data-based inferences of the hot-spot conditions, in particular the nuclear yield, ion temperature, burn duration, and volume are used for the hot-spot inference methodology described in Refs. 4 and 24. This produces hot-spot quantities including its ρR, mass, internal energy, and pressure, which are used for the Lawson ignition criteria discussed in Ref. 8 and the discussion in the following section.
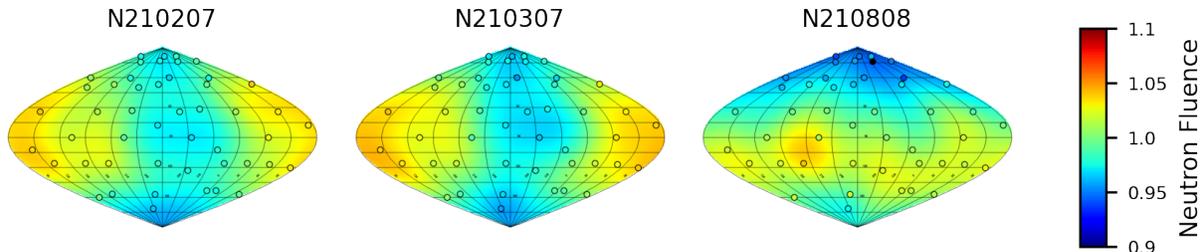
FIG. 4. Neutron emission isotropy as an Aitoff projection in target-chamber coordinates, comparing the three experiments.

III. IGNITION SIGNATURES

Herein is the first clear experimental signature that this experiment is in a new regime. In lower performance implosions where the self-heating approximately balances energy losses from bremsstrahlung x-ray emission and thermal conduction, the compression and expansion is approximately adiabatic, in such a case a $2\times$ increase in volume would decrease the pressure (PV^γ staying constant). Instead for N210808 we have both the pressure and volume increasing $\sim 2\times$ for a comparable fuel kinetic energy (see Ref. 9) which clearly indicates a substantial additional energy input to the hot spot, in this case from the fusion self-heating. This is described as a thermodynamic ignition criteria in Ref. 55. Compared to the burning-plasma experiments we see a PV^γ 'boost'[55] of $4.9^{+1.0}_{-0.9}$ ($6.7^{+1.4}_{-1.2}$) relative to shot N210207 (N210307) which is a significant change in the thermodynamic conditions driven by self-heating.

The power balance in the hot spot, which determines the evolution of the hot-spot temperature, is[11]

$$c_{\mathrm{DT}}\frac{dT_{\mathrm{th}}}{dt} = f_\alpha Q_\alpha - f_B Q_{\mathrm{B,DT}} - Q_{\mathrm{e}} - \frac{1}{m}p\frac{dV}{dt} \qquad (1)$$

where c_{DT} is the plasma heat capacity, Q_α is the alpha self-heating power from fusion where f_α is the fraction of the α energy deposited in the hot spot[56]. $Q_{B,DT}$ is the bremsstrahlung emission for equimolar DT, where the f_B factor is the fraction of the emission lost (< 1 with reabsorption, > 1 if enhanced by higher Z material in the hot spot). Q_e is the thermal conduction loss, and the last term represents PdV work done on or by the hot spot depending on the sign of dV/dt. For more details see Refs. 4 and 8.

$Q_{B,DT}$ and Q_e invariably act as loss mechanisms from the hot spot. The point at which self-heating surpasses the sum of these two loss mechanisms is the static self-heating regime, which was marginally reached in previous experiments, notably N210207 as discussed in Ref. 4. To illustrate the degree to which fusion self-heating increased on N210808 versus experiments in the burning-plasma regime, we add this igniting experiment to a burning-plasma criteria from Hurricane et al. (Ref. 57) as used in Ref. 4; this is shown in Fig. 6 (equivalent

to Fig. 3 in Ref. 4). The Hurricane criteria is written as an inequality relative to the implosion velocity (see Eq. 1 in Ref. 4) and is drawn as a contour in ρR_{hs}, T_i space (top of Fig. 6) or as a radio between the effective condition velocity and the implosion velocity ($v_{cond}/v_{imp} > 1$ corresponding to a burning plasma). This parameter effectively quadruples from the burning-plasma experiments to N210808. The self-heating boundary ($f_\alpha Q_\alpha > f_B Q_{\mathrm{B,DT}} + Q_{\mathrm{e}}$) is shown by the black dashed curve. Clearly N210808 is significantly beyond both the burning-plasma boundary (as shown by the condition's probability plot at the bottom of Fig. 6) as well as the static self-heating boundary.

Surpassing the static self-heating boundary is a necessary but not sufficient criteria for ignition because after peak compression is reached, $dV/dt > 0$ and acts as a loss mechanism. The temperature evolution is therefore determined by whether the self-heating ($f_\alpha Q_\alpha$) can overcome all of the negative (loss) terms on the right hand side of Eq. 1. The time-integrated images (Fig. 5) being larger while simulation models show that the radius at peak compression is similar[9] strongly suggests, in combination with the high hot-spot pressure, that burn occurs while the hot spot is expanding ($dV/dt > 0$) and that self-heating must dominate. This can also be seen in measurements of the fusion burn history, shown in Fig. 7 as the fusion power versus time (in power units, i.e. $m_{hs}f_\alpha Q_\alpha$). Here, we use Gaussian fits to the data with 1σ errors denoted by the shaded regions; far from the peak non-Gaussian may occur that is not captured in Fig. 7. Each measurement has been aligned relative to the simulated time of peak compression. We see that all shots have a fusion burn rate ~ 1 PW near the time of peak compression, and what is notable is the behavior after peak compression - while N210207 and N210307 increase only $\sim 2\times$, as PdV losses counteract self-heating while they expand. In contrast N210808 has the burn rate increase by more than an order of magnitude from peak compression to peak power, which can only occur for an igniting implosion where self-heating dominates the right-hand side of Eq. 1.

Fig. 8 shows additional signatures of ignition in the energy and mass in the hot spot on N210808 relative to the database of prior NIF shots (inferred using the methodology in Ref. 24). Compared to the previous high-
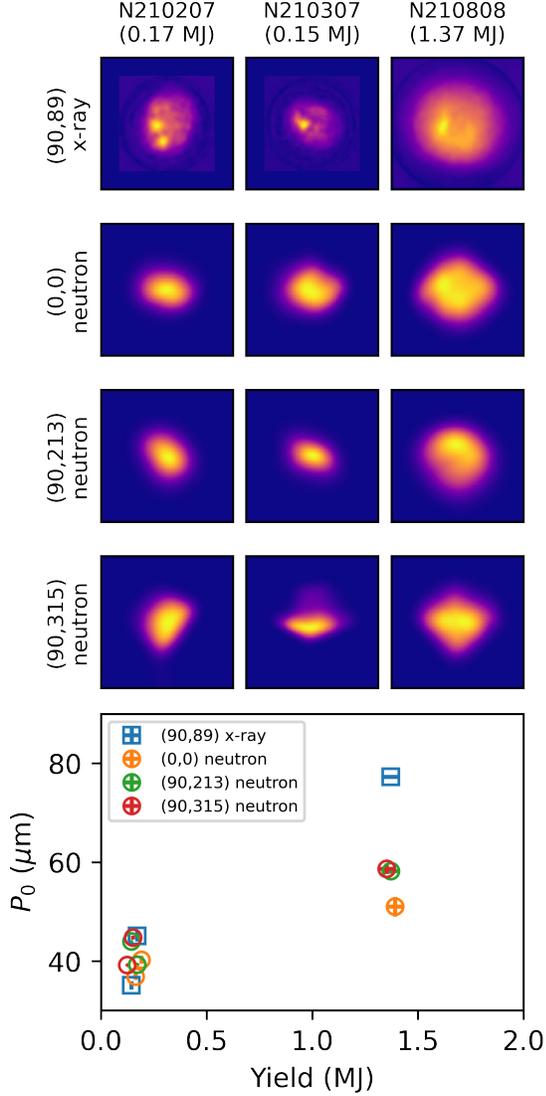
FIG. 5. Self-emission imaging data for N210808 (right) compared to predecessor experiments (N210207, N210307) using neutron or x-ray imagers. Images are shown at top, all 100×100 μm, with the diagnostic type and line of sight in target-chamber coordinates is given (θ, ϕ in degrees from the top of the target chamber) at left. The bottom plot shows the average radius (P_0, defined as the 17% emissivity contour versus the peak brightness) versus yield of the shot (with some points artificially displaced by a small amount for clarity). N210808 exhibits a substantially increased volume while simultaneously having a higher inferred pressure.

performing experiments, N210808 has $\sim 2\times$ the hot-spot mass (m_{hs}) and more than $3\times$ the energy E_{hs}. We can start with $E_{hs} = c_{DT}m_{hs}T_{hs}$ and since the self-heating is the source of energy after the initial formation of the hot spot (here, we know from the previously-discussed data that the burn is predominantly occurring after minimum
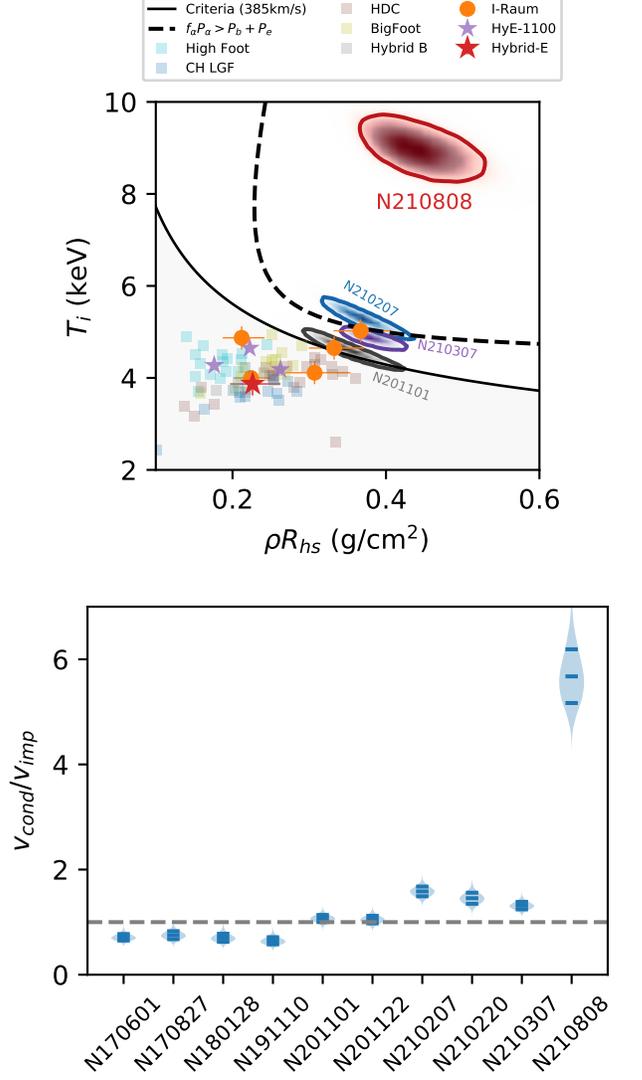
FIG. 6. Top: Hot-spot parameter space of T_i and ρR_{hs} with previous experiments, as well as N210808, shown relative to the burning-plasma criteria of Ref. 57 (black curve) and the static self-heating boundary (black dashed curve). Probabilistic distributions are shown for the Hybrid-E burning plasma experiments (N201101, gray; N210207, blue; N210307, purple) as well as N210808 in red. The bottom plot shows the burning plasma condition on velocity, normalized to the implosion velocity (> 1 corresponding to a burning plasma) for N210808 relative to previous experiments.

volume), the evolution is:

$$\frac{dE_{hs}}{dt} = c_{DT}\left(m_{hs}\frac{dT_{hs}}{dt} + \frac{dm_{hs}}{dt}T_{hs}\right). \qquad (2)$$

Using Eq. 1 with the assumption that the hot-spot mass increase is driven by the escaping α particles and thermal conductivity, [11]

$$\frac{dm_{hs}}{dt} = \frac{m_{hs}}{c_{DT}T_{hs}}\left[(1 - f_\alpha)Q_\alpha + Q_e\right], \qquad (3)$$
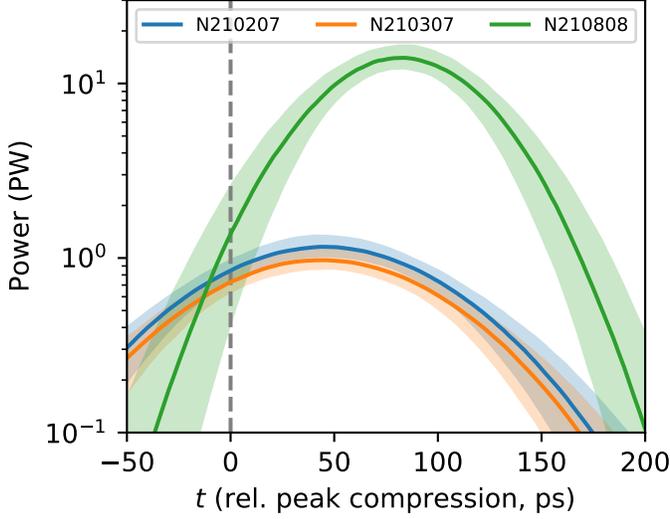
FIG. 7. Fusion power versus time, relative to peak compression ($t = 0$, gray dashed line). The shaded bands denote 1σ uncertainty.
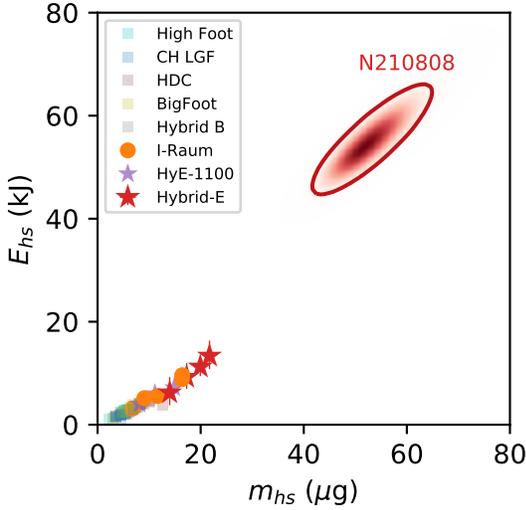
FIG. 8. Inferred hot-spot mass and energy for N210808 compared to previous shots.

$$\frac{dE_{hs}}{dt} = m_{hs}Q_\alpha - m_{hs}f_B Q_{B,DT} - p\frac{dV}{dt}. \quad (4)$$

The substantial increase in hot-spot energy and mass is therefore clear experimental evidence that the self-heating is dominating over all other power-balance terms, a signature of ignition and propagation.

This can also be seen in inferred reconstructions of the hot spot. Fig. 9 investigates the hot-spot temperature. Temporal and spatial averaged temperatures, measured from DT and DD neutron Doppler broadening, increases by $\sim 2\times$ on N210808. Using the methodology of Ref. 24, the center of Fig. 9 shows a 1-D conduction-limited profile inferred from the data, with N210808 being both hotter and larger. The right plot shows the inferred hot-spot temperature as a function of the hot-spot mass. It is clear that the amount of fuel mass which corresponds to the hot spots on N210207 and N210307 ($\sim 20-30~\mu g$) is significantly hotter on N210808, by $\sim 2\times$. In addition, N210808 exhibits a substantial mass at several keV temperatures. This is a clear signature of burn propagation, especially as the total fuel mass is $\sim 200~\mu g$, suggesting that around a third of the fuel is at fusion-relevant conditions ($\gtrsim 4$ keV) on N210808, compared to $\sim 10\%$ for the lower performing N210207 and N210307.

Hot-spot reconstructions are also performed using 3-D reconstructions of the neutron emissivity[58] combined with an isobaric model[59]. The inferred temperature versus fuel mass from these reconstructions are shown in Fig. 10, which confirms that N210808 experienced a significant level of burn propagation into the cold fuel, with a significant fraction of fuel both heated to several keV temperatures and producing substantial fractions of the total yield compared to the burning-plasma experiments (N210207, N210307).

Lastly we examine the hot-spot energy and pressure. What the energy and pressure would have been in the absence of self-heating ($E_{hs,n\alpha}$ and $P_{hs,n\alpha}$ respectively) is inferred[60]; the quantity $E_{hs,n\alpha}P_{hs,n\alpha}^2$ is a metric for ignition or performance[17, 18] and the threshold nature of ignition means that the burn-on quantity should increase rapidly as the power balance tips in favor of self heating. The data are shown in Fig. 11, with the burn-off quantities at top and burn-on at bottom compared to previous data. In each plot, contours of EP^2 are shown relative to the value achieved on N210207. In burn-off quantities EP^2 improved on N210808 by about $30-40\%$ from the predecessor (N210207), consistent with previous estimates of the gap between those burning-plasma experiments and ignition[4, 5]. In the ignition regime, self-heating dramatically increases these hot-spot quantities from their burn-off values, as seen in Fig. 11 - in the presence of self heating, EP^2 is increased by $\sim 8\times$ relative to the predecessor experiment with the $\sim 35\%$ improvement without self-heating.

We note that these hot-spot quantities are physically implausible to achieve on NIF for indirect drive designs without the presence of dominating self-heating. Here, the internal energy of the hot spot is more than $3\times$ the fuel's kinetic energy during implosion; in contrast all previous NIF experiments had the hot spot energy, at best, comparable to the initial fuel kinetic energy. The stagnation pressure is significantly higher than any previous experiment; reaching > 500 GBar pressures is only plausible to achieve with dominant self heating given the amount of work being done on the hot spot during the implosion.
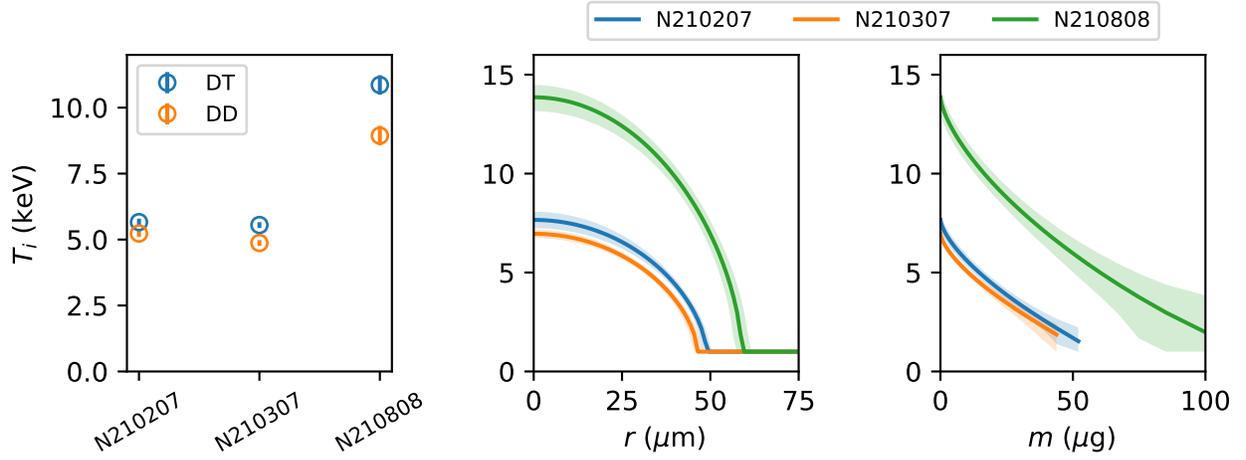
FIG. 9. Inferred temperature from neutron time of flight spectra (DT and DD, left). Using a 1-D hot-spot model the temperature as a function of radius (center) and mass (right) is inferred. For the latter two plots 1σ uncertainties are denoted by the shaded regions.
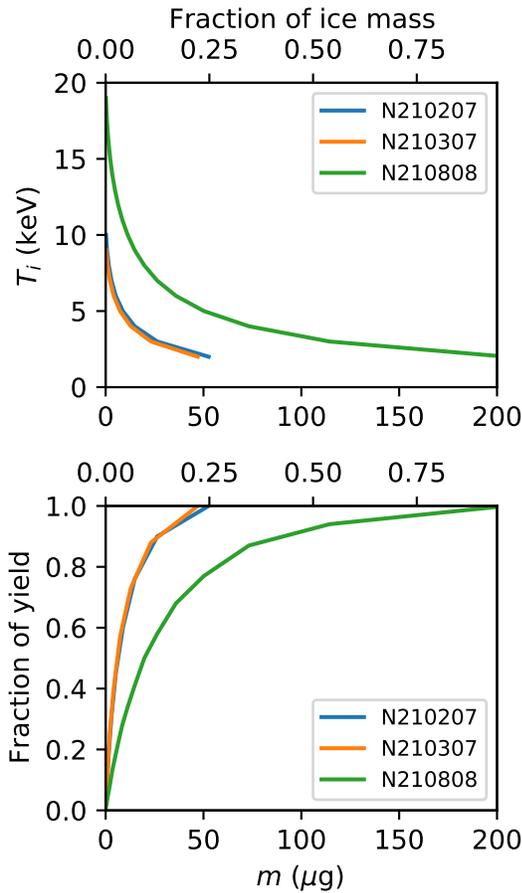
FIG. 10. 3-D reconstructions of the hot spot are also used to infer the T_i (top) and fraction of yield produced (bottom) versus fuel mass.
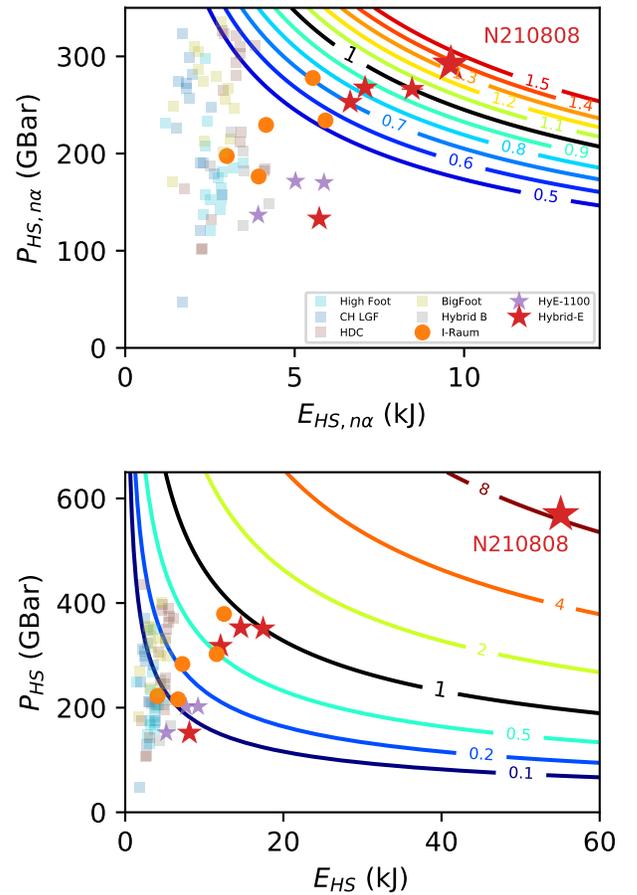
FIG. 11. Hot-spot pressure and energy, inferred without the influence of self-heating (top) and with self-heating included (bottom). Contours of constant EP^2 relative to N210207 are shown.

IV. CONCLUSION

N210808 was an ICF experiment conducted using the Hybrid E design[12, 13] in which previous experiments, in the burning-plasma regime[4, 5], were improved by reducing the implosion's coast time[9] and improving capsule quality; the combination of these changes improved the performance of this implosion by $\sim 8\times$ with it surpassing Lawson's criterion for ignition[8]. Here, we present details on the experimental improvements implemented for N210808 and we examine the data and inferred hot-spot metrics in more depth. The hot-spot energy and pressure increased dramatically from the predecessor experiments, examining the metric EP^2 the burn-off quantity increased $\sim 35\%$ while with the presence of self heating it increased $\sim 8\times$, a clear signature of the ignition process which is fundamentally a thermodynamic instability. The hot-spot energy and mass being substantially higher than the predecessors is direct evidence of the alpha heating dominating over other energy balance terms. We observe that the fusion burn rate increases more than an order of magnitude after the time of peak compression, and that burn propagation into a significant fraction of the dense fuel occurred for the first time. These observations are seen for the first time in the laboratory on N210808 and are signatures of the ignition and burn propagation process.

ACKNOWLEDGMENTS

[1] J. Nuckolls, L. Wood, A. Thiessen, and G. Zimmerman, Nature **239**, 139 (1972).
[2] J. Lindl, Phys. Plasmas **2**, 3933 (1995).
[3] E. I. Moses *et al.*, Journal of Physics: Conference Series **688**, 012073 (2016).
[4] A. Zylstra, O. Hurricane, *et al.*, Nature **601**, 542 (2022).
[5] A. Kritcher, C. Young, H. Robey, *et al.*, Nature Physics **18**, 251 (2022).
[6] J. D. Lawson, Proceedings of the Physical Society. Section B **70**, 6 (1957).
[7] NYYMMDD, YY=year, MM=month, DD=day.
[8] NIF Team, submitted to Phys. Rev. Lett. (2022).
[9] A. L. Kritcher *et al.*, submitted to Phys. Rev. Lett. (2022).
[10] O. A. Hurricane *et al.*, Phys. Plasmas **24** (2017).
[11] O. A. Hurricane *et al.*, Plasma Phys. Control. Fusion **61** (2019).
[12] A. B. Zylstra *et al.*, Phys. Rev. Lett. **126**, 025001 (2021).
[13] A. L. Kritcher *et al.*, Phys. Plasmas **28**, 072706 (2021).
[14] A. B. Zylstra *et al.*, Phys. Plasmas **27**, 092709 (2020).
[15] A. B. Zylstra *et al.*, Phys. Plasmas **21**, 112701 (2014).
[16] O. A. Hurricane *et al.*, Phys. Plasmas **27**, 062704 (2020).
[17] J. D. Lindl *et al.*, Phys. Plasmas **25**, 122704 (2018).
[18] A. Zylstra *et al.*, Nucl. Fusion **61**, 116066 (2021).
[19] J. Ralph *et al.*, "Measurements of improved hohlraum efficiency for near term burning plasma designs," (2021), APS DPP, GO04.00003.
[20] J. E. Ralph *et al.*, in preparation (2022).
[21] J. L. Kline *et al.*, Rev. Sci. Instrum. **81**, 10E321 (2010).
[22] S. Khan *et al.*, in *Target Diagnostics Physics and Engineering for Inertial Confinement Fusion*, Vol. 8505 (International Society for Optics and Photonics, 2012) p. 850505.
[23] B. Bachmann *et al.*, Phys. Rev. E **101**, 033205 (2020).
[24] A. Zylstra *et al.*, Phys. Plasmas **28**, 122703 (2021).
[25] T. Ma *et al.*, Phys. Rev. Lett. **111**, 085004 (2013).
[26] S. R. Nagel, S. W. Haan, J. R. Rygg, M. Barrios, L. R. Benedetti, D. K. Bradley, J. E. Field, B. A. Hammel, N. Izumi, O. S. Jones, S. F. Khan, T. Ma, A. E. Pak, R. Tommasini, and R. P. J. Town, Phys. Plasmas **22**, 022704 (2015), https://doi.org/10.1063/1.4907179.
[27] R. Tommasini *et al.*, Phys. Plasmas **22**, 056315 (2015).
[28] A. G. MacPhee *et al.*, Phys. Rev. E **95**, 031204 (2017).
[29] C. R. Weber *et al.*, Physics of Plasmas **27**, 032703 (2020), https://doi.org/10.1063/1.5125599.
[30] A. G. MacPhee, V. A. Smalyuk, O. L. Landen, C. R. Weber, H. F. Robey, E. L. Alfonso, J. Biener, T. Bunn, J. W. Crippen, M. Farrell, S. Felker, J. E. Field, W. W. Hsing, C. Kong, J. Milovich, A. Moore, A. Nikroo, N. Rice, M. Stadermann, and C. Wild, Phys. Plasmas **25** (2018), 10.1063/1.5025183.
[31] A. Pak *et al.*, Phys. Rev. Lett. **124**, 145001 (2020).
[32] A. L. Kritcher *et al.*, Phys. Plasmas **21** (2014).
[33] H. G. Rinderknecht, D. T. Casey, R. Hatarik, R. M. Bionta, B. J. MacGowan, P. Patel, O. L. Landen, E. P. Hartouni, and O. A. Hurricane, Phys. Rev. Lett. **124**, 145002 (2020).
[34] D. T. Casey *et al.*, Phys. Rev. Lett. **126**, 025002 (2021).
[35] B. J. MacGowan *et al.*, High Energy Density Physics **40**, 100944 (2021).
[36] J. L. Milovich *et al.*, Plasma Phys. Control. Fusion **63**, 025012 (2020).
[37] A. S. Moore, D. J. Schlossberg, E. P. Hartouni, D. Sayre, M. J. Eckart, R. Hatarik, F. Barbosa, J. Root, C. Waltz, B. Beeman, M. S. Rubery, and G. P. Grim, Review of Scientific Instruments **89**, 10I120 (2018), https://doi.org/10.1063/1.5039322.
[38] D. J. Schlossberg *et al.*, Phys. Rev. Lett. **127**, 125001 (2021).
[39] R. M. Bionta *et al.*, Rev. Sci. Instrum. **92**, 043527 (2021).
[40] K. D. Hahn, R. M. Bionta, H. Khater, E. A. Henry, A. S. Moore, D. J. Schlossberg, D. A. Barker, E. R. Casco, R. B. Ehrlich, L. Divol, J. M. Gjemso, T. B. Golod, G. P. Grim, E. P. Hartouni, J. Jeet, and S. M. Kerr, Rev. Sci. Instrum. **92**, 053543 (2021), https://doi.org/10.1063/5.0043844.
[41] R. Bionta, D. Casey, G. Grim, K. Hahn, E. Hartouni, A. Moore, and R. Nora, Bulletin of the American Physical Society **66** (2021).
[42] D. L. Bleuel *et al.*, Rev. Sci. Instrum. **83**, 10D313 (2012).
[43] M. G. Johnson *et al.*, Rev. Sci. Instrum. **83**, 10D308 (2012).
[44] J. Frenje *et al.*, Nuclear Fusion **53**, 043014 (2013).
[45] L. Ballabio, J. Källne, and G. Gorini, Nucl. Fusion **38**, 1723 (1998).
[46] V. Y. Glebov *et al.*, Rev. Sci. Instrum. **81**, 10D325 (2010).
[47] R. Hatarik *et al.*, J. Appl. Phys. **118**, 184502 (2015).
[48] H. W. Herrmann *et al.*, Rev. Sci. Instrum. **81**, 10D333 (2010).
[49] H. Geppert Kleinrath *et al.*, submitted to Rev. Sci. Instrum. (2022).
[50] T. Ma *et al.*, Rev. Sci. Instrum. **83**, 10E115 (2012).
[51] P. Volegov *et al.*, Rev. Sci. Instrum. **85**, 023508 (2014).
[52] V. Geppert Kleinrath *et al.*, to be submitted to Rev. Sci. Instrum. (2022).
[53] V. Smalyuk *et al.*, in *Penetrating Radiation Systems and Applications XII*, Vol. 8144 (International Society for Optics and Photonics, 2011) p. 81440N.
[54] C. B. Yeamans and D. L. Bleuel, Fusion Science and Technology **72**, 120 (2017).
[55] O. A. Hurricane *et al.*, Phys. Plasmas **28**, 022704 (2021).
[56] A. B. Zylstra and O. A. Hurricane, Phys. Plasmas **26**, 062701 (2019).
[57] O. A. Hurricane *et al.*, Phys. Plasmas **26**, 052704 (2019).
[58] P. L. Volegov, S. H. Batha, D. N. Fittinghoff, C. R. Danly, V. Geppert-Kleinrath, C. H. Wilde, and A. B. Zylstra, Rev. Sci. Instrum. **92**, 033508 (2021).
[59] L. Divol, in *APS Division of Plasma Physics Meeting Abstracts*, Vol. 2019 (2019) pp. DI3–001.
[60] P. K. Patel *et al.*, Phys. Plasmas **27**, 050901 (2020).